

PeakNet: An Autonomous Bragg Peak Finder with Deep Neural Networks

Cong Wang¹, Po-Nan Li², Jana Thayer¹, and Chun Hong Yoon^{1,*}

¹*Linac Coherent Light Source, SLAC National Accelerator Laboratory, Menlo Park, CA, USA.*

²*Department of Electrical Engineering, Stanford University, Stanford, CA, USA.*

* *Corresponding author: yoons82@slac.stanford.edu*

June 30, 2023

Abstract

Serial crystallography at X-ray free electron laser (XFEL) and synchrotron facilities has experienced tremendous progress in recent times enabling novel scientific investigations into macromolecular structures and molecular processes. However, these experiments generate a significant amount of data posing computational challenges in data reduction and real-time feedback. Bragg peak finding algorithm is used to identify useful images and also provide real-time feedback about hit-rate and resolution. Shot-to-shot intensity fluctuations and strong background scattering from buffer solution, injection nozzle and other shielding materials make this a time-consuming optimization problem. Here, we present PeakNet, an autonomous Bragg peak finder that utilizes deep neural networks. The development of this system 1) eliminates the need for manual algorithm parameter tuning, 2) reduces false-positive peaks by adjusting to shot-to-shot variations in strong background scattering in real-time, 3) eliminates the laborious task of manually creating bad pixel masks and the need to store these masks per event since these can be regenerated on demand. PeakNet also exhibits exceptional runtime efficiency, processing a 1920×1920 pixel image around 90 ms on an NVIDIA 1080 Ti GPU, with the potential for further enhancements through parallelized analysis or GPU stream processing. PeakNet is well-suited for expert-level real-time serial crystallography data analysis at high data rates.

1 Introduction

Serial crystallography with X-ray free electron lasers (XFEL) has enabled radiation damage-free structural determination of macromolecules at room temperature, an approach commonly known as *diffraction-before-destruction* (Neutze et al., 2000; Chapman et al., 2006, 2011). Time-resolved serial femtosecond crystallography at XFEL facilities, like the Linac Coherent Light Source (LCLS), allows the investigation of biochemical reactions with femtosecond-scale time resolution which has led to many significant structural studies (Kupitz et al., 2014; Nango et al., 2016; Pande et al., 2016; Young et al., 2016; Suga et al., 2017; Kern et al., 2018; Ibrahim et al., 2020; Suga et al., 2020) since the first published work at LCLS (Aquila et al., 2012). In the meantime, the data rate at XFEL facilities have also gradually increased from hundreds of Hz to the MHz range, with the European X-ray Free Electron Laser (EuXFEL) being the first MHz facility available to users and LCLS-II set to launch in 2023.

At the MHz data rate, novel real-time data analysis approaches are needed to tackle two major challenges that arise in SFX experiments, namely data reduction and real time feedback. The standard approach for data reduction is vetoing events where the x-ray pulse did not “hit” the sample. Typically, hit finding in serial crystallography utilizes Bragg peak finding algorithms implemented in such programs as Cheetah (Barty et al., 2014), DIALS (Winter et al., 2018), and Psocake (Yoon, 2020). Additionally, a deep neural network-based hit finder for serial crystallography has been reported to achieve a processing rate of 1.3 kHz by analyzing downsized 180×180 images on a single GPU (Ke et al., 2018). Real-time feedback in serial crystallography experiments plays a crucial role by providing users with important information about the experimental conditions. This enables them to make timely decisions that optimize the data collection process. For instance, it is essential to fine-tune the hit rate to maximize the utilization of samples. Additionally, it is important to monitor factors such as the current diffraction limit, crystalline mosaicity, reciprocal space coverage, and other relevant parameters over time. Therefore, relying solely on hit finding is insufficient to gain the necessary insights, making real-time Bragg peak finding vital for delivering prompt and comprehensive feedback.

In this work, we introduce PeakNet, a solution that effectively addresses the challenge of autonomously and efficiently identifying Bragg peaks in high data rate scenarios. Our approach involves transforming the peak

finding problem into a semantic segmentation task, where different regions within diffraction images are classified and segmented using a deep neural network. PeakNet autonomously detects Bragg peaks while effectively identifying shot-to-shot variations of strong non-Bragg scattering artifacts, eliminating the need for human intervention. Subsequently, connected areas of pixels are examined and treated as individual peaks, a task easily accomplished through connected component analysis (Weaver, 1985). The coordinates of the peaks are determined by calculating the center of mass of all pixels belonging to each identified peak. Notably, the entire peak finding process is performed on GPUs, offering a cost-effective solution for achieving low latency.

2 Related work

Reliable and automatic peak finding algorithms have undergone multiple iterations of development. An early approach involved utilizing template matching (Wilkinson et al., 1988) based on libraries of peak shapes, but this method was found to be slow and inefficient in runtime, especially when dealing with peaks with low signal-to-noise ratios (SNR). The main obstacle lies in the localization of peaks and the tuning of user parameters for pattern matching, compounded by the difficult task of developing a comprehensive library of peak shapes. Another influential approach employed region-growing techniques (Bolotovskiy et al., 1995; Barty et al., 2014) to detect pixel areas with high skewness. In the context of serial crystallography with XFEL sources, the efficacy of this method was diminished due to the lack of sufficient data to provide reliable statistics, rendering it susceptible to outliers and less adept in analyzing weak peaks at higher scattering angles, which are essential for achieving atomic resolution in structure determination.

While template matching and region-growing techniques require users to provide prior information like threshold values, Robust Peak Finder (RPF) (Hadian-Jazi et al., 2017, 2021) has demonstrated proficient peak finding capabilities with minimal user input. This technique utilizes the Modified Selective Statistical Estimator (MSSE) method to segment background pixels and actual peaks. Furthermore, the RPF method can also parallelize the processing of diffraction patterns, making it ideal for real-time data analysis.

Psocake is a software program specifically designed to streamline high throughput data reduction and analysis of XFEL experiments, and is routinely used at SLAC National Accelerator laboratory (SLAC). The built-in

peak-finding algorithm (Shin et al., 2018) includes calibrating raw analog digital units (ADUs); applying optional background correction and bad pixel masks; identifying possible peaks; calculating their SNR; determining Bragg spot sizes; and selecting peaks based on size, total intensity and SNR.

In recent years, neural network models have emerged as a promising avenue for Bragg peak finding. BraggNet (Sullivan et al., 2019) is the first method that demonstrates proficiency of neural network models, specifically U-Net (Ronneberger et al., 2015), in accurately segmenting peak pixels, including weak peaks, from background pixels in neutron crystallography data. BraggNet employed simulated peaks to create training datasets, which underwent a number of preprocessing steps, including centering and cropping to a specific size and adding Poisson noise. It should be noted that BraggNet works on a single peak at a time within a small 32 by 32 window, which deviates significantly from conventional Bragg peak finding tasks that require extracting peak positions from images typically with hundreds or thousands of pixels along one dimension. Furthermore, another neural network method for Bragg peak analysis was detailed in the work of BraggNN (Liu et al., 2021), emphasizing the refinement of Bragg peak positions without the need for explicit fitting of a profile function, such as the pseudo-Voigt profile. Likewise, BraggNN works on a single peak at a time within a 11 by 11 window, performing regression to two variables representing the peak position. To the best of our knowledge, no existing neural network based peak-finding models have demonstrated the ability to detect multiple peaks, which is the primary goal we strive to achieve with PeakNet.

3 Methods

The current peak finding process of PeakNet comprises of two steps, as depicted in Fig. 1. First, a segmentation map is obtained from the input image using a deep neural network. Subsequently, peak positions are determined based on the generated segmentation map using connected component analysis (Weaver, 1985). Importantly, PeakNet has the capability to process inputs with arbitrary image sizes in batches, enabling efficient analysis.

In this section, our focus is to provide a comprehensive description of the underlying deep neural network components in PeakNet. We will specifically discuss the network architecture, data augmentation techniques, and the loss function employed during the training process. Furthermore, we will emphasize the use of

iterative data curation in addressing the outlier problem.

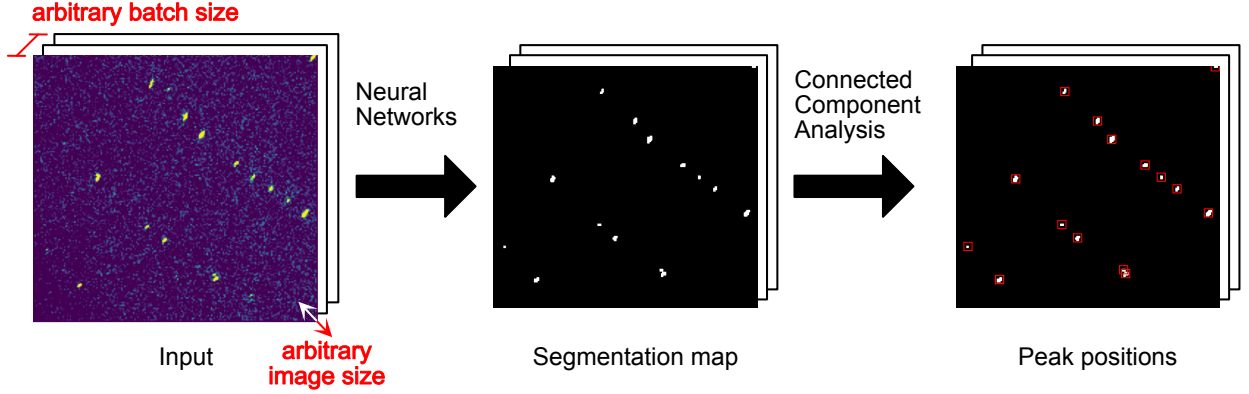


Figure 1: The peak finding process of PeakNet consists of two steps: (1) obtaining a segmentation map from the input using the underlying deep neural network; (2) identifying peak positions based on the generated segmentation map using connected component analysis. It is worth noting that PeakNet is capable of accommodating input with arbitrary image sizes and batch sizes.

3.1 Neural network architecture

The underlying neural network architecture of PeakNet is illustrated in Figure 2 (a). It employs a residual attention U-Net architecture, comprising three main components: a feature extraction “backbone”, a feature fusion “neck”, and a single prediction “head”. The feature extraction “backbone” utilizes multiple residual double convolutional blocks to extract multi-resolution features, as visualized in Figure 2 (b). In the feature fusion “neck”, low-resolution features are merged with high-resolution features using gated feature fusion blocks, as depicted in 2 (c). Each block incorporates an attention gate that enhances shared features within both low and high-resolution feature maps. The resulting combined features from each gated feature fusion block are then rearranged by a subsequent residual double convolutional block. Finally, to accomplish the segmentation task, the prediction “head” leverages fused features from the “neck” and generates a prediction map encompassing three distinct labels: background, Bragg peak, and artifact scattering. The “head” itself consists of a 1×1 convolutional layer followed by a softmax function.

Our neural network architecture is primarily based on the original “Attention U-Net” design (Oktay et al., 2018). However, we want to point out that the three-component design, consisting of the “backbone”, “neck”

and “head”, offers the flexibility to replace these components with different architectures. For instance, the “backbone” can be substituted with a ResNet (He et al., 2016), while the “neck” can be replaced with other multi-resolution feature fusion methods like feature pyramid networks (FPN) (Lin et al., 2017) or bidirectional feature pyramid networks (BiFPN) (Tan et al., 2020). Additionally, the “head” can be extended to perform additional tasks, if desired, such as predicting the likelihood of the input image being indexable. This modular approach provides flexibility and allows for customization based on specific requirements.

3.2 Focal loss as the loss function

One main technical issue in training neural networks for Bragg peak segmentation is the extreme peak-background class imbalance (e.g., less than $1 : 10^3$), resulting in reduced prediction accuracy. This may not pose as a problem in previous peak finders like BraggNet, which operates on a much smaller area of 32×32 , PeakNet is trained on larger detectors, such as the Rayonix MX340-XFEL detector with a dimension of 1920×1920 pixels even after 4×4 pixel binning. To mitigate the label imbalance, we employ a categorical focal loss to address the problem (Lin et al., 2018).

$$\text{CFL} = - \sum_{i=1}^N \sum_{j=1}^C \alpha_j \cdot y_j^{(i)} \cdot (1 - \hat{p}_j^{(i)})^\gamma \cdot \log \hat{p}_j^{(i)}, \quad (1)$$

$$\hat{p}_j^{(i)} = f_\theta(x_j^{(i)}) \quad (2)$$

where CFL stands for categorical focal loss, α_j is a balancing factor for each class, $y_j^{(i)}$ is the ground truth label of the j -th class for the i -th pixel. $p_j^{(i)}$ is the predicted probability of the j -th class for the i -th pixel, calculated by the neural network f parameterized by θ given input image $x_j^{(i)}$ with N number of pixels and C categories. γ is a parameter controlling the extent to which the weight of well-classified examples, such as background pixels, is reduced. In our neural network training, we chose $\gamma = 2.0$, essentially, this means $(1 - \hat{p}_j^{(i)})^\gamma$ is solely responsible for down-weighting easy examples, as $\hat{p}_j^{(i)}$ is usually large in this case. Finding the ideal values for α can be a delicate process with only marginal returns, as highlighted in the original focal loss study (Lin et al., 2018). In order to fully utilize focal loss, we decided to use a fixed trivial value of $\alpha = 1.2$ for all examples, primarily for the sake of completeness. This choice essentially treats α as a simple

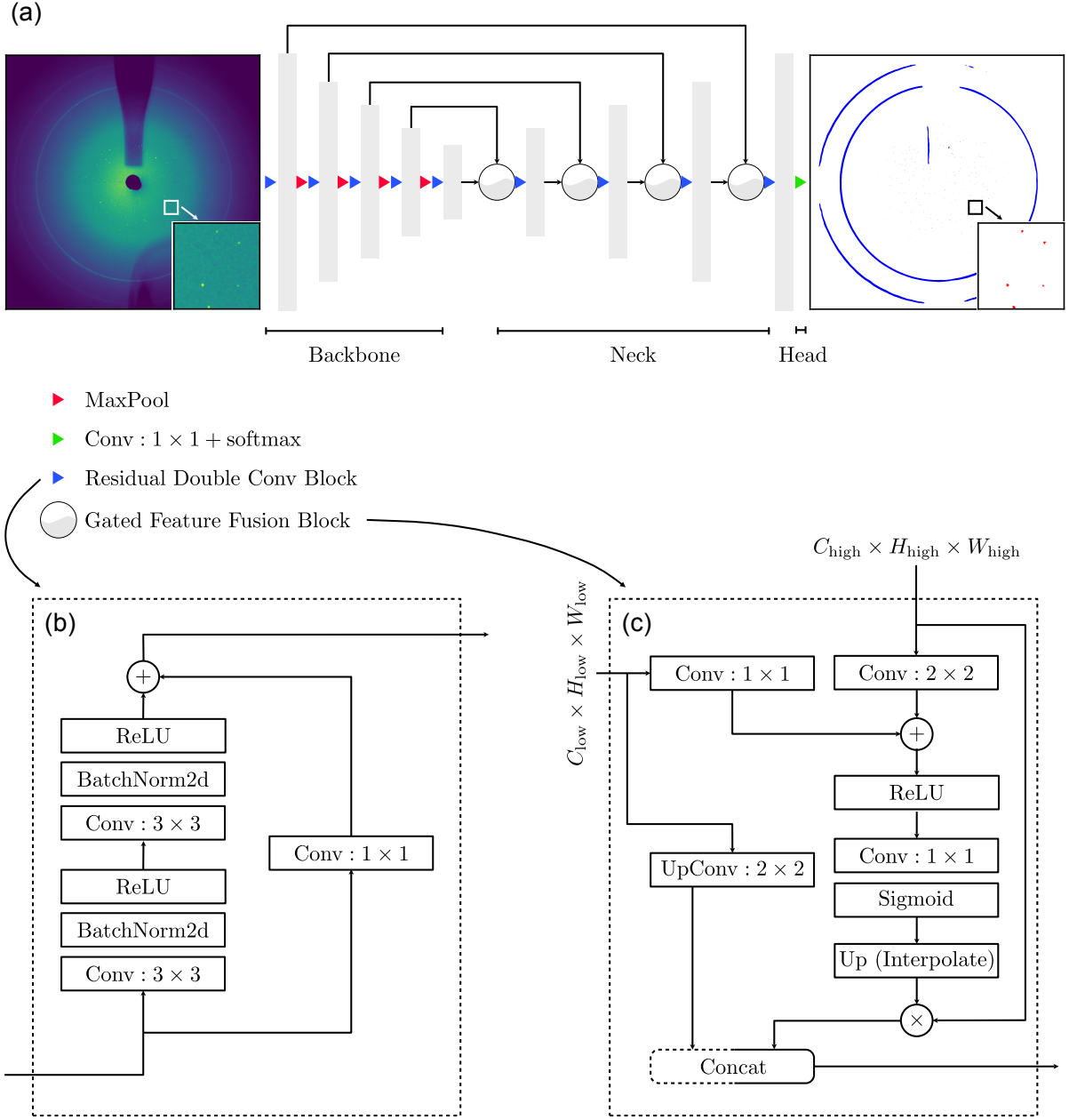


Figure 2: Neural network architecture: Attention U-Net with residual connections. (a) Overall end-to-end network architecture. (b) Residual double convolutional block. (c) Gated feature fusion block for merging multi-resolution features.

scaling factor without significant impact. In most cases, the sum of all α_j values, denoted as $\sum_{j=1}^C \alpha_j$, sums to 1.

3.3 Data augmentation

We applied three data augmentation techniques to each diffraction pattern in our dataset, including random in-plane rotation, random shifting in both horizontal and vertical directions and random masking. Random in-plane rotation and shifting augment the training data, reducing the model’s tendency to memorize features at specific locations. This variability promotes more generalized feature extraction and improved generalization performance. Random masking involves randomly obscuring parts of the input data, forcing the model to learn other relevant features that enhance its predictive capabilities during training. 50 rectangular masks with random sizes between 80 and 120 were positioned randomly. The result of applying data augmentation to an arbitrary example is shown in Fig. 3.

3.4 Dataset improvement and correction

PeakNet employs a data-driven approach to accurately identify Bragg peaks, requiring dataset improvement and correction to enhance performance. This contrasts with model-driven approaches that primarily entail direct model modification to improve capabilities. Fig. 4 illustrates a feedback loop for iterative dataset improvement and correction.

The process begins with the preparation of a source dataset, often accomplished through a combination of algorithmic and manual data labeling. Subsequently, the deep neural networks within PeakNet are trained on this dataset to learn how to accurately detect peaks. Following training, the model is deployed to predict peaks on previously unseen data, and its performance is thoroughly evaluated. During this evaluation, instances that notably worsen the performance of PeakNet are identified. To address these limitations, we either correct low-quality labels predicted by the neural networks or, alternatively, acquire additional data that closely resemble these challenging instances and carefully annotate them. Finally, we merge these newly labeled instances into the training set and retrain the model, thereby improving its overall performance.

Interestingly, during the initial pass of this iterative process, PeakNet showed limited performance when dealing with images containing relatively low levels of photons. However, by obtaining and annotating these images, we were able to enhance the training dataset and, as a result, significantly improve the predictive performance of PeakNet.

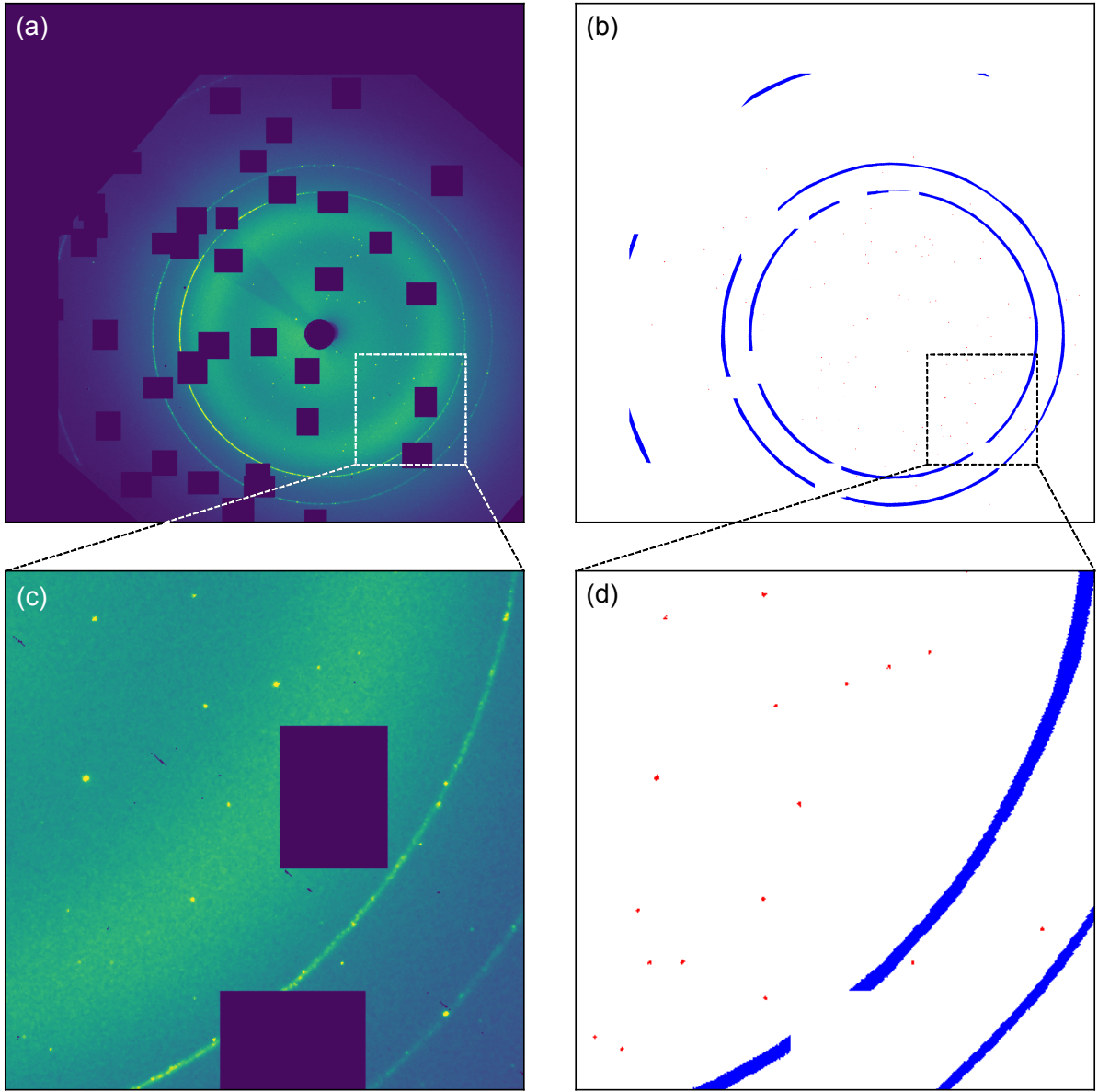


Figure 3: Illustration of data augmentation on an input image. (a) Augmented image with random in-plane rotation, shift, and masking. (b) its corresponding labeled segmentation map. (c, d) Zoomed-in views of (a) and (b), respectively. The segmentation label distinguishes red pixels as peaks and blue pixels as artifact scattering, attributed to scattering from metal shielding and injection nozzle.

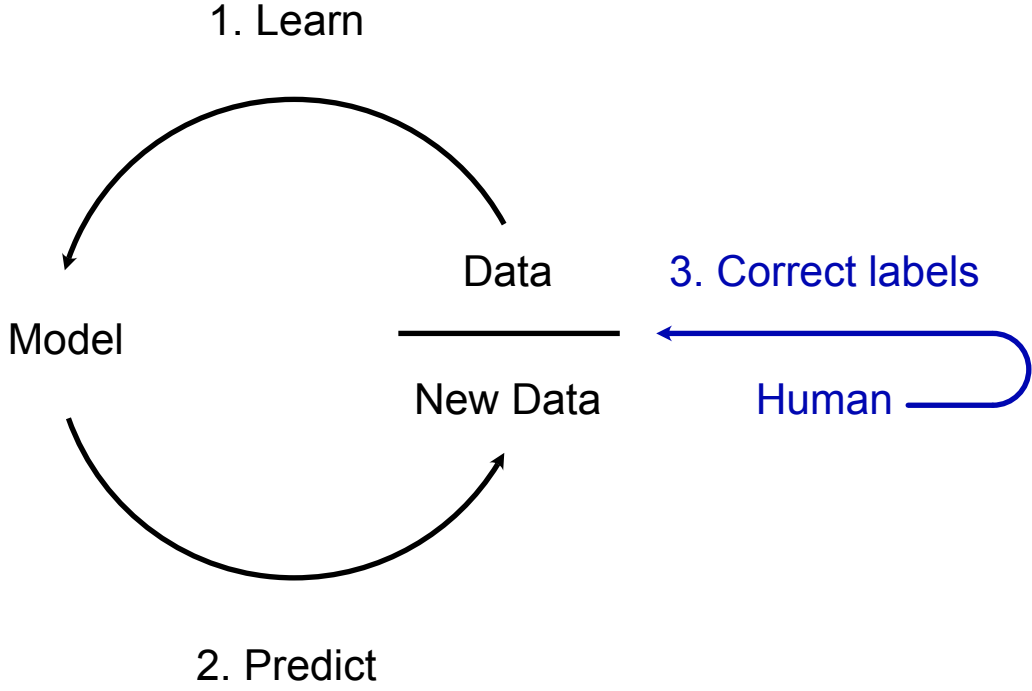


Figure 4: The three step process of iterative dataset and model improvement. (1) Model learns from training data. (2) Model predictions reveal potential areas of improvement. (3) Correct low-quality training labels or acquire additional examples of challenging instances.

4 Results

The primary goal of PeakNet is to autonomously detect Bragg peaks in diffraction images, devoid of any user input, such as algorithmic parameter tuning or manual artifact masking. We implemented a two-step approach for peak detection, employing deep neural networks to perform semantic segmentation, which was subsequently followed by connected component analysis to extract image coordinates of Bragg peaks. In this section, we begin by introducing the datasets used for training, validating, and testing PeakNet. Next, we present the evaluation results that demonstrate the predictive performance of PeakNet. Finally, we showcase its auto-masking capability and runtime efficiency.

4.1 Dataset

We obtained X-ray diffraction images from two experiments conducted at the Macromolecular Femtosecond Crystallography (MFX) instrument within LCLS. The primary dataset utilized for training and evaluating PeakNet is “mfx13016” (Run number: 28,31-34, 36-38), which contains diverse biological samples, e.g. thaumatin and proteinase, and this experiment was originally used for automated drop dispensing research (Su et al., 2021). These diffraction images were recorded on a Rayonix MX340-XFEL detector with a dimension of 1920×1920 , downsized by a factor of 4 to accommodate a higher readout rate.

The dataset “mfx13016” exhibits a notable ring-like background scattering accompanied by bright Bragg peak-like spots located on the rings. This characteristic presents two primary challenges for crystallography data analysis: increased difficulty in crystal indexing due to false-positive peaks and inaccurate integration results caused by artifact scattering. The current best practice involves manual masking of these artifact scattering, enabling data analysis to proceed as if they are absent, but this process is time-consuming and can not adjust to shot-to-shot variations in the artifacts in real-time. Additionally, the final outcomes often hinge on the expertise of the individuals conducting the data processing, resulting in biases, scalability limitations, lack of standardization, and the possibility of human errors. Nevertheless, the inherent challenges presented by this dataset offer an exceptional opportunity to showcase the autonomous peak finding capability of PeakNet.

The neural network training dataset consists of 98 Rayonix images in run 28 of “mfx13016”, which includes thaumatin samples, and an additional 37 images sampled from an internal LCLS experimental dataset related to therapeutics development associated with SARS-CoV-2. Incorporating the SARS-CoV-2 dataset aims to educate PeakNet about the presence of images without artifact rings, diversifying its understanding of different data characteristics. Nonetheless, all these images used for neural network training have a dimension of 1920×1920 and they are divided into an 80% training set and a 20% validation set. The final test dataset for evaluating the model comprises all images in run 31-34 and run 36-38 of “mfx13016”.

4.2 Evaluating PeakNet’s predictive performance

The peak finding performance of peak finders is evaluated through three key indicators from a user’s standpoint: the number of successfully indexed hits, the indexing rate, and the merging statistics. For our evaluation, we utilized the CrystFEL software suite (White et al., 2012) to perform crystal indexing, integration, and merging tasks. We use Psocake’s peak finder as a baseline in this evaluation.

4.2.1 Indexing results

PeakNet and manually fine-tuned Psocake exhibit comparable peak finding performance in terms of the number of hits and the number of indexed images, as shown in Table 1. However, we emphasize that while PeakNet operates entirely autonomously, Psocake’s performance is contingent upon manual parameter fine-tuning and manual artifact scattering masking. For example, an earlier work (Su et al., 2021), which processed the same experimental data, reported significantly lower hit count and indexed image count. Consequently, this highlights PeakNet’s advantage in user-independent expert-level data processing.

Moreover, while users might prioritize the absolute number of indexed images as a more straightforward metric, the indexing rate provides valuable insights into the method’s efficiency. Both metrics jointly offer a more comprehensive evaluation of the peak finding method. In the case of PeakNet, both consistently high number of indexed images and high indexing rate testify to its effective and reliable autonomous peak finding process.

4.2.2 Merging statistics

Merging statistics confirms PeakNet’s robust performance in terms of consistency and quality in data processing. For the thaumatin (TH) sample, PeakNet demonstrates marginally superior performance in terms of R-split values, correlation coefficients, $I/\sigma(I)$ values, redundancy, and completeness, achieving these results autonomously. Notably, the R-split value for thaumatin is slightly lower for PeakNet (0.2605 vs. 0.2732), suggesting slightly better internal consistency. Similarly, correlation coefficients for PeakNet are marginally higher ($CC_1/2$: 0.9434 vs. 0.9368; CC^* : 0.9853 vs. 0.9835), indicating a minor advantage in the precision of measurements.

Table 1: Comparison of crystal indexing results for different methods on the test dataset. The table shows the number of hits, number of indexed hits, and indexing rates for PeakNet, Psocake (fine-tuned) and Psocake (Su 2021). The “Run (Samples)” column lists the specific run numbers and biological samples (TH: thaumatin; PK: proteinase).

Methods	Run (Samples)	31 (TH)	32 (TH)	33 (TH)	34 (TH)	36 (TH)	37 (PK)	38 (PK)
PeakNet	Number of hits	1205	3248	5797	3949	1184	1030	1223
	Number of indexed	860	2856	3433	2401	919	953	1169
	Indexing rate	0.71	0.88	0.59	0.61	0.78	0.93	0.96
Psocake (fine-tuned)	Number of hits	1193	3087	5769	3926	917	1070	1212
	Number of indexed	849	2657	3375	2364	760	1005	1202
	Indexing rate	0.71	0.86	0.59	0.60	0.83	0.94	0.99
Psocake (Su2021)	Number of hits	1083	2454	5604	3756	363	683	771
	Number of indexed	271	1094	963	770	266	569	709
	Indexing rate	0.25	0.45	0.17	0.21	0.73	0.83	0.92

Table 2: Comparison of merging statistics between PeakNet and fine-tuned Psocake. Thaumatin (TH) results were merged from run 31, 32, 33, 34 and 36. Proteinase (PK) results were merged from run 37 and 38.

Sample	Methods	R-split	CC _{1/2}	CC*	$I/\sigma(I)$	Resolution range (Å)	Redundancy	Completeness
TH	PeakNet	0.2605	0.9434	0.9853	2.0590	1.45-27.93	76.05	0.9594
	Psocake	0.2732	0.9368	0.9835	2.0277	1.01-31.32	72.20	0.9367
Sample	Methods	R-split	CC _{1/2}	CC*	$I/\sigma(I)$	Resolution range (Å)	Redundancy	Completeness
PK	PeakNet	0.7711	0.2234	0.6043	1.135	1.45-26.98	16.36	0.8668
	Psocake	0.7589	0.1900	0.5650	0.974	1.45-30.04	17.83	0.8365

However, for the proteinase (PK) sample, the performance comparison is mixed. Although PeakNet lags slightly behind manually fine-tuned Psocake in terms of R-split and redundancy, it outperforms in CC_{1/2}, CC*, $I/\sigma(I)$, and completeness values. This reinforces the effectiveness of PeakNet in achieving respectable results across varied sample types, without any manual intervention or parameter fine-tuning.

Overall, PeakNet demonstrates comparable performance to a manually fine-tuned Psocake for two distinct samples, showcasing its potential for autonomous peak finding with consistent results. By reducing dependence on the expertise of individuals, which can have considerable variation, PeakNet offers a promising user-independent solution. Notably, despite primarily being trained on PK samples, PeakNet maintains robust and versatile performance, indicating its broad applicability and effectiveness in handling diverse datasets.

4.3 Auto-masking: predicting scattering artifacts

Auto-masking functionality in PeakNet represents a significant advancement in the automated processing of diffraction images. The underlying neural network architecture enables PeakNet to autonomously discern and segregate pixel regions affected by scattering artifacts, such as distinct ring-like structures produced by metal shielding used to reduce air scatter and/or liquid jet nozzle scattering. This capability circumvents the need for manual masking in the peak finding process and the need to store a binary mask used for each

event which is needed for crystal indexing/integration, thereby optimizing the efficiency of crystallographic data processing.

Fig. 5 provides a comparative visualization of PeakNet’s effectiveness in accurately segmenting regions with bright pixels induced by scattering artifacts under various conditions. Images without ring artifacts are also included in the visualization, reassuring that PeakNet does not generate or “hallucinate” ring artifacts where they do not exist. This visual representation serves as tangible evidence of PeakNet’s adeptness in discriminating and processing pertinent features, regardless of the contextual complexities.

Furthermore, while evaluating PeakNet’s auto-masking feature on intended input images, we explored its behavior on unintended inputs, providing insights into its robustness and generalizability. Fig. 6 depicts illustrative examples of PeakNet predicting artifact scattering patterns in silver behenate scattering captured on various detectors. Silver behenate is a popular calibrant used to determine the detector position relative to the beam based on the known ring spacing. Surprisingly, PeakNet reliably identifies the characteristic scattering ring structures present in silver behenate images. This observation provides compelling evidence once again, further demonstrating the robust predictive capability of PeakNet in accurately recognizing artifact scattering patterns. As a result, it reinforces that effectiveness of PeakNet’s auto-masking feature and the potential to automatically optimize the diffraction geometry.

4.4 Runtime efficiency

Peak finding can pose a significant computational demand, particularly in high data rate experiments, highlighting the critical importance of an efficient peak finding algorithm. A comparative analysis of runtime performance demonstrates the greater efficiency of PeakNet compared to other commonly used Psocake peak finder.

When processing Rayonix images with 1920×1920 pixels, PeakNet achieved a significantly reduced processing time of 90 milliseconds per event on an NVIDIA 1080 Ti GPU. In contrast, Psocake required 176 milliseconds per event when executed on an Intel E5-2620 CPU. Another peak finding method, RPF (robust peak finder), operating on Intel E5-2698, is reported to require 120 milliseconds but on a smaller AGIPD 1M images (Hadian-Jazi et al., 2021). This result clearly demonstrates that PeakNet not only delivers robust Bragg

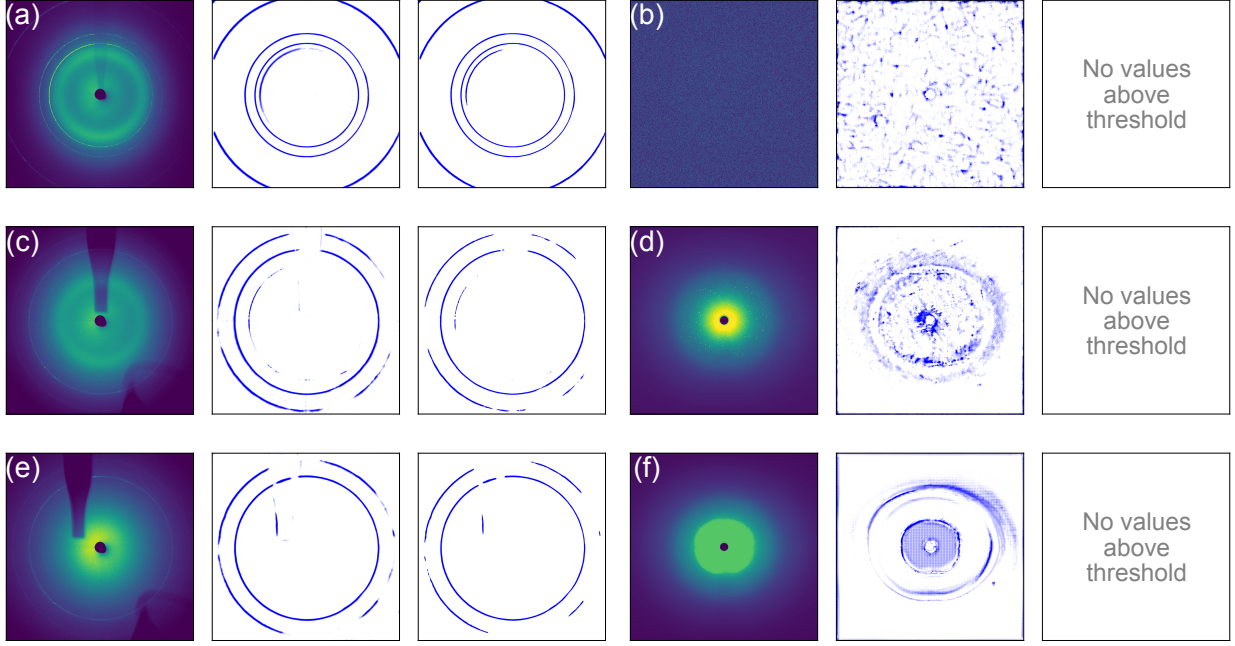


Figure 5: Examples of auto-masking using PeakNet. Each panel contains three images: the original image, the segmentation map used for masking, and the resulting mask after thresholding. Panels (a), (c) and (e) show three different scenarios with artifact scattering rings. Panels (b), (d) and (f) visualize the response of PeakNet on images without any artifact scattering rings.

peak finding results in an autonomous fashion, but also exhibits remarkable runtime efficiency.

5 Conclusions

PeakNet exhibits exceptional capabilities in autonomous Bragg peaks finding without requiring user input or intervention, such as algorithmic parameter tuning or manual artifact masking. The predictive performance of PeakNet in peak finding proves to be comparable to, if not better than, manually fine-tuned Psocake with user-supplied masks. An integral feature of PeakNet, auto-masking, significantly enhances its ability to autonomously identify and process artifact scattering patterns. Moreover, the efficiency of PeakNet is exemplified by its impressive runtime performance, surpassing commonly used peak finders like Psocake and RPF. Parallel processing with GPU streaming can potentially improve the runtime efficiency even further. In conclusion, PeakNet offers a robust, versatile, and efficient solution that operates independently of user

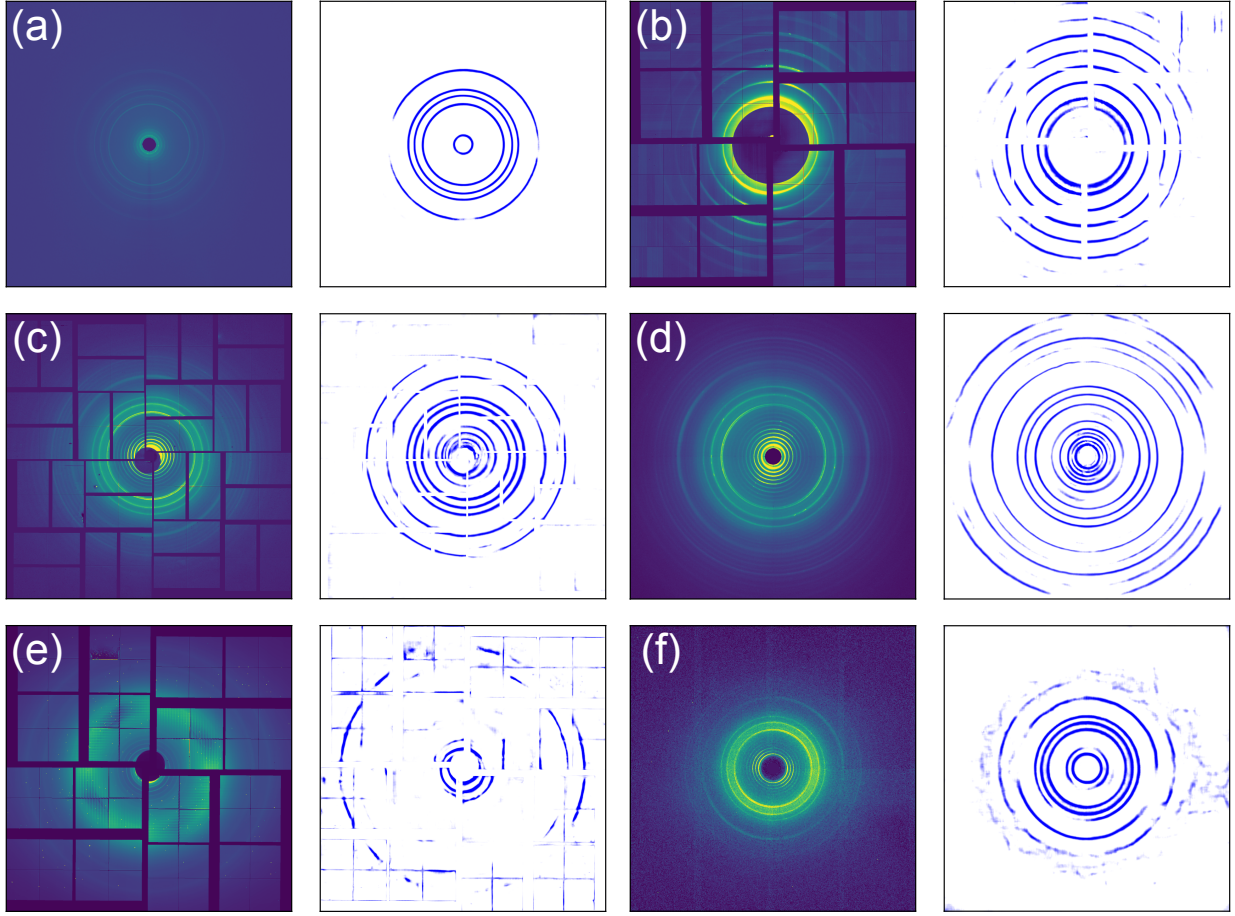


Figure 6: Examples of identifying scattering rings in silver behenate images using PeakNet.

input, thereby holding significant potential for optimizing crystallographic data processing at high data rates.

Acknowledgment

Earlier versions utilizing YOLO and U-Net models were built and tested by P.L and C.H.Y. The experiments were designed by C.W with inputs from J.B.T and C.H.Y. C.W implemented the residual attention U-Net, prepared the datasets, labeled experimental data, and trained and evaluated the refined neural network model. The manuscript was written by C.W and C.H.Y with input from all authors. This material is based upon work supported by the U.S. Department of Energy, Office of Science, Office of Basic Energy Sciences under Award Number FWP-100643. Use of the Linac Coherent Light Source (LCLS), SLAC National Accelerator Laboratory, is supported by the U.S. Department of Energy, Office of Science, Office of Basic

Table 3: The runtime performance of diffraction image analysis algorithms measured on Rayonix images containing 3.7 megapixels. We measured runtime performance of Psocake and PeakNet directly using Rayonix images. For reference purposes, we also included another peak finding method RPF (Hadian-Jazi et al., 2017, 2021) and two classification methods for X-ray diffraction data reduction. RPF runtime performance was originally measured on AGIPD 1M (Allahgholi et al., 2019).

Methods	Hardware	Image size	Time (ms/event)
PeakNet	NVIDIA 1080 Ti	1920×1920	90.0
Psocake	Intel E5-2620	1920×1920	175.5
RPF	Intel E5-2698	1024×1024	120.0

Energy Sciences under Contract No.DE-AC02-76SF00515. C.W acknowledges the assistance provided by ChatGPT from OpenAI in refining the language and enhancing the readability of this paper.

References

- Aschkan Allahgholi, Julian Becker, Annette Delfs, Roberto Dinapoli, Peter Goettlicher, Dominic Greifenberg, Beat Henrich, Helmut Hirsemann, Manuela Kuhn, Robert Klanner, Alexander Klyuev, Hans Krueger, Sabine Lange, Torsten Laurus, Alessandro Marras, Davide Mezza, Aldo Mozzanica, Magdalena Niemann, Jennifer Poehlsen, Joern Schwandt, Igor Sheviakov, Xintian Shi, Sergej Smoljanin, Lothar Steffen, Jolanta Sztuk-Dambietz, Ulrich Trunk, Qingqing Xia, Mourad Zeribi, Jiaguo Zhang, Manfred Zimmer, Bernd Schmitt, and Heinz Graafsma. The Adaptive Gain Integrating Pixel Detector at the European XFEL. *Journal of Synchrotron Radiation*, 26(1):74–82, January 2019. ISSN 1600-5775. doi: 10.1107/S1600577518016077.
- Andrew Aquila, Mark S. Hunter, R. Bruce Doak, Richard A. Kirian, Petra Fromme, Thomas A. White, Jakob Andreasson, David Arnlund, Saša Bajt, Thomas R. M. Barends, Miriam Barthelmess, Michael J. Bogan, Christoph Bostedt, Hervé Bottin, John D. Bozek, Carl Caleman, Nicola Coppola, Jan Davidsson, Daniel P. DePonte, Veit Elser, Sascha W. Epp, Benjamin Erk, Holger Fleckenstein, Lutz Foucar, Matthias

Frank, Raimund Fromme, Heinz Graafsma, Ingo Grotjohann, Lars Gumprecht, Janos Hajdu, Christina Y. Hampton, Andreas Hartmann, Robert Hartmann, Stefan Hau-Riege, Günter Hauser, Helmut Hirsemann, Peter Holl, James M. Holton, André Hömke, Linda Johansson, Nils Kimmel, Stephan Kassemeyer, Faton Krasniqi, Kai-Uwe Kühnel, Mengning Liang, Lukas Lomb, Erik Malmerberg, Stefano Marchesini, Andrew V. Martin, Filipe R.N.C. Maia, Marc Messerschmidt, Karol Nass, Christian Reich, Richard Neutze, Daniel Rolles, Benedikt Rudek, Artem Rudenko, Ilme Schlichting, Carlo Schmidt, Kevin E. Schmidt, Joachim Schulz, M. Marvin Seibert, Robert L. Shoeman, Raymond Sierra, Heike Soltau, Dmitri Starodub, Francesco Stellato, Stephan Stern, Lothar Strüder, Nicusor Timneanu, Joachim Ullrich, Xiaoyu Wang, Garth J. Williams, Georg Weidenspointner, Uwe Weierstall, Cornelia Wunderer, Anton Barty, John C. H. Spence, and Henry N. Chapman. Time-resolved protein nanocrystallography using an X-ray free-electron laser. *Optics Express*, 20(3):2706, January 2012. ISSN 1094-4087. doi: 10.1364/OE.20.002706.

Anton Barty, Richard A. Kirian, Filipe R. N. C. Maia, Max Hantke, Chun Hong Yoon, Thomas A. White, and Henry Chapman. *Cheetah* : Software for high-throughput reduction and analysis of serial femtosecond X-ray diffraction data. *Journal of Applied Crystallography*, 47(3):1118–1131, June 2014. ISSN 1600-5767. doi: 10.1107/S1600576714007626.

R. Bolotovskiy, M. A. White, A. Darovsky, and P. Coppens. The ‘Seed-Skewness’ Method for Integration of Peaks on Imaging Plates. *Journal of Applied Crystallography*, 28(2):86–95, April 1995. ISSN 0021-8898. doi: 10.1107/S0021889894009696.

Henry N. Chapman, Anton Barty, Michael J. Bogan, Sébastien Boutet, Matthias Frank, Stefan P. Hau-Riege, Stefano Marchesini, Bruce W. Woods, Saša Bajt, W. Henry Benner, Richard A. London, Elke Plönjes, Marion Kuhlmann, Rolf Treusch, Stefan Düsterer, Thomas Tschentscher, Jochen R. Schneider, Eberhard Spiller, Thomas Möller, Christoph Bostedt, Matthias Hoener, David A. Shapiro, Keith O. Hodgson, David van der Spoel, Florian Burmeister, Magnus Bergh, Carl Caleman, Gösta Hultdt, M. Marvin Seibert, Filipe R. N. C. Maia, Richard W. Lee, Abraham Szöke, Nicusor Timneanu, and Janos Hajdu. Femtosecond diffractive imaging with a soft-X-ray free-electron laser. *Nature Physics*, 2(12):839–843, December 2006. ISSN 1745-2473, 1745-2481. doi: 10.1038/nphys461.

Henry N. Chapman, Petra Fromme, Anton Barty, Thomas A. White, Richard A. Kirian, Andrew Aquila, Mark S. Hunter, Joachim Schulz, Daniel P. DePonte, Uwe Weierstall, R. Bruce Doak, Filipe R. N. C. Maia, Andrew V. Martin, Ilme Schlichting, Lukas Lomb, Nicola Coppola, Robert L. Shoeman, Sascha W. Epp, Robert Hartmann, Daniel Rolles, Artem Rudenko, Lutz Foucar, Nils Kimmel, Georg Weidenspointner, Peter Holl, Mengning Liang, Miriam Barthelmess, Carl Caleman, Sébastien Boutet, Michael J. Bogan, Jacek Krzywinski, Christoph Bostedt, Saša Bajt, Lars Gumprecht, Benedikt Rudek, Benjamin Erk, Carlo Schmidt, André Hömke, Christian Reich, Daniel Pietschner, Lothar Strüder, Günter Hauser, Hubert Gorke, Joachim Ullrich, Sven Herrmann, Gerhard Schaller, Florian Schopper, Heike Soltau, Kai-Uwe Kühnel, Marc Messerschmidt, John D. Bozek, Stefan P. Hau-Riege, Matthias Frank, Christina Y. Hampton, Raymond G. Sierra, Dmitri Starodub, Garth J. Williams, Janos Hajdu, Nicusor Timneanu, M. Marvin Seibert, Jakob Andreasson, Andrea Rocker, Olof Jönsson, Martin Svenda, Stephan Stern, Karol Nass, Robert Andritschke, Claus-Dieter Schröter, Faton Krasniqi, Mario Bott, Kevin E. Schmidt, Xiaoyu Wang, Ingo Grotjohann, James M. Holton, Thomas R. M. Barends, Richard Neutze, Stefano Marchesini, Raimund Fromme, Sebastian Schorb, Daniela Rupp, Marcus Adolph, Tais Gorkhover, Inger Andersson, Helmut Hirsemann, Guillaume Potdevin, Heinz Graafsma, Björn Nilsson, and John C. H. Spence. Femtosecond X-ray protein nanocrystallography. *Nature*, 470(7332):73–77, February 2011. ISSN 0028-0836, 1476-4687. doi: 10.1038/nature09750.

Marjan Hadian-Jazi, Marc Messerschmidt, Connie Darmanin, Klaus Giewekemeyer, Adrian P. Mancuso, and Brian Abbey. A peak-finding algorithm based on robust statistical analysis in serial crystallography. *Journal of Applied Crystallography*, 50(6):1705–1715, December 2017. ISSN 1600-5767. doi: 10.1107/S1600576717014340.

Marjan Hadian-Jazi, Alireza Sadri, Anton Barty, Oleksandr Yefanov, Marina Galchenkova, Dominik Oberthuer, Dana Komadina, Wolfgang Brehm, Henry Kirkwood, Grant Mills, Raphael de Wijn, Romain Letrun, Marco Kloos, Mohammad Vakili, Luca Gelisio, Connie Darmanin, Adrian P. Mancuso, Henry N. Chapman, and Brian Abbey. Data reduction for serial crystallography using a robust peak finder. *Journal of Applied Crystallography*, 54(5):1360–1378, October 2021. ISSN 1600-5767. doi: 10.1107/S1600576721007317.

Kaiming He, Xiangyu Zhang, Shaoqing Ren, and Jian Sun. Deep Residual Learning for Image Recognition. In *2016 IEEE Conference on Computer Vision and Pattern Recognition (CVPR)*, pages 770–778, Las Vegas, NV, USA, June 2016. IEEE. ISBN 978-1-4673-8851-1. doi: 10.1109/CVPR.2016.90.

Mohamed Ibrahim, Thomas Fransson, Ruchira Chatterjee, Mun Hon Cheah, Rana Hussein, Louise Lassalle, Kyle D. Sutherlin, Iris D. Young, Franklin D. Fuller, Sheraz Gul, In-Sik Kim, Philipp S. Simon, Casper de Lichtenberg, Petko Chernev, Isabel Bogacz, Cindy C. Pham, Allen M. Orville, Nicholas Saichek, Trent Northen, Alexander Batyuk, Sergio Carbajo, Roberto Alonso-Mori, Kensuke Tono, Shigeki Owada, Asmit Bhowmick, Robert Bolotovskiy, Derek Mendez, Nigel W. Moriarty, James M. Holton, Holger Dobbek, Aaron S. Brewster, Paul D. Adams, Nicholas K. Sauter, Uwe Bergmann, Athina Zouni, Johannes Messinger, Jan Kern, Vittal K. Yachandra, and Junko Yano. Untangling the sequence of events during the $S_2 \rightarrow S_3$ transition in photosystem II and implications for the water oxidation mechanism. *Proceedings of the National Academy of Sciences*, 117(23):12624–12635, June 2020. ISSN 0027-8424, 1091-6490. doi: 10.1073/pnas.2000529117.

Tsung-Wei Ke, Aaron S. Brewster, Stella X. Yu, Daniela Ushizima, Chao Yang, and Nicholas K. Sauter. A convolutional neural network-based screening tool for X-ray serial crystallography. *Journal of Synchrotron Radiation*, 25(3):655–670, May 2018. ISSN 1600-5775. doi: 10.1107/S1600577518004873.

Jan Kern, Ruchira Chatterjee, Iris D. Young, Franklin D. Fuller, Louise Lassalle, Mohamed Ibrahim, Sheraz Gul, Thomas Fransson, Aaron S. Brewster, Roberto Alonso-Mori, Rana Hussein, Miao Zhang, Lacey Douthit, Casper de Lichtenberg, Mun Hon Cheah, Dmitry Shevela, Julia Wersig, Ina Seuffert, Dimosthenis Sokaras, Ernest Pastor, Clemens Weninger, Thomas Kroll, Raymond G. Sierra, Pierre Aller, Agata Butryn, Allen M. Orville, Mengning Liang, Alexander Batyuk, Jason E. Koglin, Sergio Carbajo, Sébastien Boutet, Nigel W. Moriarty, James M. Holton, Holger Dobbek, Paul D. Adams, Uwe Bergmann, Nicholas K. Sauter, Athina Zouni, Johannes Messinger, Junko Yano, and Vittal K. Yachandra. Structures of the intermediates of Kok’s photosynthetic water oxidation clock. *Nature*, 563(7731):421–425, November 2018. ISSN 0028-0836, 1476-4687. doi: 10.1038/s41586-018-0681-2.

Christopher Kupitz, Shibom Basu, Ingo Grotjohann, Raimund Fromme, Nadia A. Zatsepin, Kimberly N.

- Rendek, Mark S. Hunter, Robert L. Shoeman, Thomas A. White, Dingjie Wang, Daniel James, Jay-How Yang, Danielle E. Cobb, Brenda Reeder, Raymond G. Sierra, Haiguang Liu, Anton Barty, Andrew L. Aquila, Daniel Deponete, Richard A. Kirian, Sadia Bari, Jesse J. Bergkamp, Kenneth R. Beyerlein, Michael J. Bogan, Carl Caleman, Tzu-Chiao Chao, Chelsie E. Conrad, Katherine M. Davis, Holger Fleckenstein, Lorenzo Galli, Stefan P. Hau-Riege, Stephan Kassemeyer, Hartawan Laksmono, Mengning Liang, Lukas Lomb, Stefano Marchesini, Andrew V. Martin, Marc Messerschmidt, Despina Milathianaki, Karol Nass, Alexandra Ros, Shatabdi Roy-Chowdhury, Kevin Schmidt, Marvin Seibert, Jan Steinbrener, Francesco Stellato, Lifen Yan, Chunhong Yoon, Thomas A. Moore, Ana L. Moore, Yulia Pushkar, Garth J. Williams, Sébastien Boutet, R. Bruce Doak, Uwe Weierstall, Matthias Frank, Henry N. Chapman, John C. H. Spence, and Petra Fromme. Serial time-resolved crystallography of photosystem II using a femtosecond X-ray laser. *Nature*, 513(7517):261–265, September 2014. ISSN 0028-0836, 1476-4687. doi: 10.1038/nature13453.
- Tsung-Yi Lin, Piotr Dollár, Ross Girshick, Kaiming He, Bharath Hariharan, and Serge Belongie. Feature Pyramid Networks for Object Detection, April 2017.
- Tsung-Yi Lin, Priya Goyal, Ross Girshick, Kaiming He, and Piotr Dollár. Focal Loss for Dense Object Detection, February 2018.
- Zhengchun Liu, Hemant Sharma, Jun-Sang Park, Peter Kenesei, Antonino Miceli, Jonathan Almer, Rajkumar Kettimuthu, and Ian Foster. BraggNN: Fast X-ray Bragg Peak Analysis Using Deep Learning. *arXiv:2008.08198 [cs, eess]*, June 2021.
- Eriko Nango, Antoine Royant, Minoru Kubo, Takanori Nakane, Cecilia Wickstrand, Tetsunari Kimura, Tomoyuki Tanaka, Kensuke Tono, Changyong Song, Rie Tanaka, Toshi Arima, Ayumi Yamashita, Jun Kobayashi, Toshiaki Hosaka, Eiichi Mizohata, Przemyslaw Nogly, Michihiro Sugahara, Daewoong Nam, Takashi Nomura, Tatsuro Shimamura, Dohyun Im, Takaaki Fujiwara, Yasuaki Yamanaka, Byeonghyun Jeon, Tomohiro Nishizawa, Kazumasa Oda, Masahiro Fukuda, Rebecka Andersson, Petra Båth, Robert Dods, Jan Davidsson, Shigeru Matsuoka, Satoshi Kawatake, Michio Murata, Osamu Nureki, Shigeki Owada, Takashi Kameshima, Takaki Hatsui, Yasumasa Joti, Gebhard Schertler, Makina Yabashi, Ana-

- Nicoleta Bondar, Jörg Standfuss, Richard Neutze, and So Iwata. A three-dimensional movie of structural changes in bacteriorhodopsin. *Science*, 354(6319):1552–1557, December 2016. ISSN 0036-8075, 1095-9203. doi: 10.1126/science.aah3497.
- Richard Neutze, Remco Wouts, David van der Spoel, Edgar Weckert, and Janos Hajdu. Potential for biomolecular imaging with femtosecond X-ray pulses. *Nature*, 406(6797):752–757, August 2000. ISSN 0028-0836, 1476-4687. doi: 10.1038/35021099.
- Ozan Oktay, Jo Schlemper, Loic Le Folgoc, Matthew Lee, Mattias Heinrich, Kazunari Misawa, Kensaku Mori, Steven McDonagh, Nils Y. Hammerla, Bernhard Kainz, Ben Glocker, and Daniel Rueckert. Attention U-Net: Learning Where to Look for the Pancreas, May 2018.
- Kanupriya Pande, Christopher D. M. Hutchison, Gerrit Groenhof, Andy Aquila, Josef S. Robinson, Jason Tenboer, Shibom Basu, Sébastien Boutet, Daniel P. DePonte, Mengning Liang, Thomas A. White, Nadia A. Zatsepin, Oleksandr Yefanov, Dmitry Morozov, Dominik Oberthuer, Cornelius Gati, Ganesh Subramanian, Daniel James, Yun Zhao, Jake Koralek, Jennifer Brayshaw, Christopher Kupitz, Chelsie Conrad, Shatabdi Roy-Chowdhury, Jesse D. Coe, Markus Metz, Paulraj Lourdu Xavier, Thomas D. Grant, Jason E. Koglin, Gihan Ketawala, Raimund Fromme, Vukica Šrajer, Robert Henning, John C. H. Spence, Abbas Ourmazd, Peter Schwander, Uwe Weierstall, Matthias Frank, Petra Fromme, Anton Barty, Henry N. Chapman, Keith Moffat, Jasper J. van Thor, and Marius Schmidt. Femtosecond structural dynamics drives the trans/cis isomerization in photoactive yellow protein. *Science*, 352(6286):725–729, May 2016. ISSN 0036-8075, 1095-9203. doi: 10.1126/science.aad5081.
- Olaf Ronneberger, Philipp Fischer, and Thomas Brox. U-Net: Convolutional Networks for Biomedical Image Segmentation. *arXiv:1505.04597 [cs]*, May 2015.
- Hocheol Shin, Seungnam Kim, and Chun Hong Yoon. Data Analysis using Psocake at PAL-XFEL. *Journal of the Korean Physical Society*, 73(1):16–20, July 2018. ISSN 0374-4884, 1976-8524. doi: 10.3938/jkps.73.16.
- Zhen Su, Joshua Cantlon, Lacey Douthit, Max Wiedorn, Sébastien Boutet, Jan Kern, Chun Hong Yoon, and Daniel DePonte. Serial crystallography using automated drop dispensing. *Journal of Synchrotron Radiation*, 28(5):1386–1392, September 2021. ISSN 1600-5775. doi: 10.1107/S1600577521006160.

Michihiro Suga, Fusamichi Akita, Michihiro Sugahara, Minoru Kubo, Yoshiki Nakajima, Takanori Nakane, Keitaro Yamashita, Yasufumi Umena, Makoto Nakabayashi, Takahiro Yamane, Takamitsu Nakano, Mamoru Suzuki, Tetsuya Masuda, Shigeyuki Inoue, Tetsunari Kimura, Takashi Nomura, Shinichiro Yonekura, Long-Jiang Yu, Tomohiro Sakamoto, Taiki Motomura, Jing-Hua Chen, Yuki Kato, Takumi Noguchi, Kensuke Tono, Yasumasa Joti, Takashi Kameshima, Takaki Hatsui, Eriko Nango, Rie Tanaka, Hisashi Naitow, Yoshinori Matsuura, Ayumi Yamashita, Masaki Yamamoto, Osamu Nureki, Makina Yabashi, Tetsuya Ishikawa, So Iwata, and Jian-Ren Shen. Light-induced structural changes and the site of O=O bond formation in PSII caught by XFEL. *Nature*, 543(7643):131–135, March 2017. ISSN 0028-0836, 1476-4687. doi: 10.1038/nature21400.

Michihiro Suga, Atsuhiko Shimada, Fusamichi Akita, Jian-Ren Shen, Takehiko Tosha, and Hiroshi Sugimoto. Time-resolved studies of metalloproteins using X-ray free electron laser radiation at SACLA. *Biochimica et Biophysica Acta (BBA) - General Subjects*, 1864(2):129466, February 2020. ISSN 03044165. doi: 10.1016/j.bbagen.2019.129466.

Brendan Sullivan, Rick Archibald, Jahaun Azadmanesh, Venu Gopal Vandavasi, Patricia S. Langan, Leighton Coates, Vickie Lynch, and Paul Langan. BraggNet: Integrating Bragg peaks using neural networks. *Journal of Applied Crystallography*, 52(4):854–863, August 2019. ISSN 1600-5767. doi: 10.1107/S1600576719008665.

Mingxing Tan, Ruoming Pang, and Quoc V. Le. EfficientDet: Scalable and Efficient Object Detection, July 2020.

James R. Weaver. Centrosymmetric (Cross-Symmetric) Matrices, Their Basic Properties, Eigenvalues, and Eigenvectors. *The American Mathematical Monthly*, 92(10):711, December 1985. ISSN 00029890. doi: 10.2307/2323222.

Thomas A. White, Richard A. Kirian, Andrew V. Martin, Andrew Aquila, Karol Nass, Anton Barty, and Henry N. Chapman. *CrystFEL* : A software suite for snapshot serial crystallography. *Journal of Applied Crystallography*, 45(2):335–341, April 2012. ISSN 0021-8898. doi: 10.1107/S0021889812002312.

C. Wilkinson, H. W. Khamis, R. F. D. Stansfield, and G. J. McIntyre. Integration of single-crystal reflections using area multidetectors. *Journal of Applied Crystallography*, 21(5):471–478, October 1988. ISSN 0021-8898. doi: 10.1107/S0021889888005400.

Graeme Winter, David G. Waterman, James M. Parkhurst, Aaron S. Brewster, Richard J. Gildea, Markus Gerstel, Luis Fuentes-Montero, Melanie Vollmar, Tara Michels-Clark, Iris D. Young, Nicholas K. Sauter, and Gwyndaf Evans. *DIALS* : Implementation and evaluation of a new integration package. *Acta Crystallographica Section D Structural Biology*, 74(2):85–97, February 2018. ISSN 2059-7983. doi: 10.1107/S2059798317017235.

Chun Hong Yoon. Psocake: GUI for Making Data Analysis a Piece of Cake. In *Handbook on Big Data and Machine Learning in the Physical Sciences*, pages 169–178. World Scientific Publishing Co Pte Ltd, May 2020.

Iris D. Young, Mohamed Ibrahim, Ruchira Chatterjee, Sheraz Gul, Franklin D. Fuller, Sergey Koroidov, Aaron S. Brewster, Rosalie Tran, Roberto Alonso-Mori, Thomas Kroll, Tara Michels-Clark, Hartawan Laksmono, Raymond G. Sierra, Claudiu A. Stan, Rana Hussein, Miao Zhang, Lacey Douthit, Markus Kubin, Casper de Lichtenberg, Long Vo Pham, Håkan Nilsson, Mun Hon Cheah, Dmitriy Shevela, Claudio Saracini, Mackenzie A. Bean, Ina Seuffert, Dimosthenis Sokaras, Tsu-Chien Weng, Ernest Pastor, Clemens Weninger, Thomas Fransson, Louise Lassalle, Philipp Bräuer, Pierre Aller, Peter T. Docker, Babak Andi, Allen M. Orville, James M. Glowacki, Silke Nelson, Marcin Sikorski, Diling Zhu, Mark S. Hunter, Thomas J. Lane, Andy Aquila, Jason E. Koglin, Joseph Robinson, Mengning Liang, Sébastien Boutet, Artem Y. Lyubimov, Monarin Uervirojnangkoorn, Nigel W. Moriarty, Dorothee Liebschner, Pavel V. Afonine, David G. Waterman, Gwyndaf Evans, Philippe Wernet, Holger Dobbek, William I. Weis, Axel T. Brunger, Petrus H. Zwart, Paul D. Adams, Athina Zouni, Johannes Messinger, Uwe Bergmann, Nicholas K. Sauter, Jan Kern, Vittal K. Yachandra, and Junko Yano. Structure of photosystem II and substrate binding at room temperature. *Nature*, 540(7633):453–457, December 2016. ISSN 0028-0836, 1476-4687. doi: 10.1038/nature20161.